Scrape off layer heat transport and divertor power deposition of pellet induced ELMs

RP Wenninger[1], TH Eich[2], GTA Huysmans[3], PT Lang[2], S Devaux[2], S Jachmich[4], F Köchl[5] and JET EFDA Contributors[6]

JET-EFDA, Culham Science Centre, Abingdon, OX14 3DB, UK

[1]Universitätssternwarte der Ludwig-Maximilians-Universität, 81679 München, Germany

[2]Max-Planck-Institut für Plasmaphysik, EURATOM Association, Garching, Germany

[3]CEA Cadarache, Association Euratom/CEA, 13108, St Paul-Lez-Durance, France

[4]Laboratory for Plasma Physics, Ecole Royal Militaire/Koninklijke Militaire School, B-1000 Brussels, Belgium

[5]Association EURATOM-ÖAW, Atominstitut, TU Wien, 1020 Wien, Austria

[6]See the Appendix of F. Romanelli et al., Proceedings of the 23rd IAEA Fusion Energy Conference 2010, Daejeon, Korea

E-mail: ronald.wenninger@ipp.mpg.de

Abstract. Results on key aspects of scrape off layer (SOL) heat transport and divertor power load associated with pellet induced ELMs in comparison to spontaneous ELMs are presented. We focus on the 3D structure of the SOL heat transport by revealing the footprints of power load on the divertor target. Additionally, the time scales of ELM loss and consecutive energy transport in the SOL towards the divertor target of pellet induced ELMs are discussed.

By employing a toroidal magnetic field (B_T) scan we achieve evidence that a toroidally asymmetric divertor power deposition structure is extending to positions exceptional far off the strike line and exceeding toroidaly localized the power flux density at the strike line. Field lines tracing is used to predict correctly for the full B_T scan the position of the divertor power footprint of an ELM filament through the pellet injection trajectory. Consistently the divertor heat flux modeled with the non-linear MHD-code JOREK features in addition to the toroidally symmetric component peaking at the strike line a spiral like structure joining this symmetric component from higher radii. For the investigated JET discharges we conclude that the divertor heat loads due to pellet induced ELM consist out of two components. First, the toroidaly symmetric peak heat load at the strike line is comparable to the one of spontaneous ELMs. Secondly, the toroidal asymmetric component is found to be higher by $\sim$ 30% at a toroidal position defined by the SOL field line pitch.

1. Introduction

In the high confinement regime (H-mode) tokamak plasmas exhibit repetitive edge instabilities called edge localised modes (ELMs) [1]. It is currently assumed that a

reliable control technique for ELMs is mandatory for the success of ITER [2, 3, 4]. Experiments at ASDEX Upgrade have shown that deuterium ice pellets reaching the pedestal top reliably and instantly induce ELMs up to frequencies twice the natural ELM frequency [5]. Having this in mind for the design of next step fusion devices and the preparation of successful operation of those it is of paramount importance to gain information about the process of inducing ELMs by pellets and reaching some level of understanding in this process. It has been observed for spontaneous (non-triggered) ELMs that the product of ELM frequency and ELM loss energy is roughly constant and equals about 20% to 30% of the heating power [6]. This paper investigates the ELM loss energy for pellet induced ELMs and compares the observed divertor target heat loads to the ones observed for spontaneous ELMs. Furthermore the timescales and wetted area associated with ELM divertor heat deposition are compared between spontaneous and pellet induced ELMs.

Pellet injection has a technically given toroidal asymmetric nature. Due to this the question arises, if the spatial structure of the perturbation associated with pellet induced ELMs in comparison to spontaneous ELMs features a corresponding higher toroidal asymmetry in the SOL and in the divertor. Dedicated experimental investigations as well as nonlinear modeling provide information according to this.

The paper is organized in the following way: In section 2 the experimental conditions, the pellet injection system, the divertor infrared system as central diagnostic and important analysis methods are described. A typical evolution of a pellet induced ELM is described in section 3. Section 4 compares thermal energy losses and radiated energy for spontaneous and pellet induced ELMs. In section 5 we present experimental and theoretical findings with respect to toroidal asymmetry of divertor deposition and SOL power flux density of pellet induced ELMs. In section 6 we present a detailed comparison analysis of ELM divertor power deposition aspects for spontaneous and pellet induced ELMs. Section 7 summarizes and discusses the obtained results.

2. Experimental arrangement

2.1. Experimental Conditions

Table 2.1 summarizes a number of plasma parameters of the discharges that are analyzed in this paper. The abbreviations in table 1 mean (#) number of the discharge, (Δt) time interval of flat top phase used for data analysis, (n_{av}) density averaged over plasma volume and investigated time interval, (I_P) plasma current, ($|B_T|$) absolute value of toroidal magnetic field, (δ_{up} respectively δ_{low}) upper respectively lower triangularity at the separatrix, (q_{95}) safety factor at the surface of 95% of the poloidal magnetic flux at the separatrix, (P_{tot}) total additional heating power, (W_{mhd}) plasma stored energy obtained from equilibrium reconstruction and (Gas) total gas injection rate. In all discharges the main additional heating source is neutral beam heating. Partially ion cyclotron resonance heating (76697: 0.3MW, 77420 (1^{st} phase): 1.0MW, 79573: 1.5MW)

and lower hybrid current drive (76697: 0.6MW from 21,5s) are also applied.
Whereas discharges 76697 and 78606 have a fixed toroidal magnetic field and plasma current, we make use in discharges 79573 (77695) of a pre-programmed scan of the absolute value of the toroidal magnetic field from 2.2T to 2.8T (2.2-3.2T) while keeping the plasma current fixed.

Table 1. Overview of the main parameters of the discharges analyzed in this paper

#	Δt [s]	n_{av} [$10^{19}m^{-3}$]	I_P [MA]	$\|B_T\|$ [T]	δ_{up} [1]	δ_{low} [1]	q_{95} [1]	P_{tot} [MW]	W_{mhd} [MJ]	Gas [$10^{22}s^{-1}$]
76697	18-22	8.1	2.5	2.7	0.42	0.40	3.4	13 (18-20s) 16.5 (20-22s)	5.2	0.32
77420	17.6-18.4	5.3	2.5	2.7	0.18	0.35	3.6	11	4.2	0
	21.9-22.6	3.3	2.0	2.4	0.22	0.24	4.0	0	0.7	0
77695	17-22	4.4	2.0	2.2-3.2	0.20	0.35	2.2-5.8	15	3.6-4.6	0
78606	16-22	4.7	2.0	2.3	0.23	0.30	3.8	10.5	4.2	0
79573	14-21	4.5	2.0	2.2-2.8	0.18	0.34	3.6-4.8	9.5 (14-20s) 8 (20-21s)	2.6-3.6	0.08

2.2. Pellet Injection System

Since 2008 JET is equipped with a High Frequency Pellet Injector (HFPI), which is extruding one or two Deuterium ice rods, cutting these into pellets of cylindrical shape and accelerating the pellets via a high pressure Helium gas pulse [7]. The injector has been designed for two modes of operation: Pellet ELM pacing and plasma fueling. In the pellet ELM pacing mode the injector is operating with two ice rods in order to produce relatively small pellets at high repetition rates, while in the plasma fueling mode the injector is extruding a single ice rod, which is cut into relatively large pellets. A number of specifics from the original design of the injector can be seen in table 2.

Table 2. Design parameters of JETs High Frequency Pellet Injector

Mode of operation	Pellet ELM pacing	Plasma fueling
Pellet diameter [mm]	1.2-1.8	3-5
Number of D-atoms	$0.07 - 0.13 \times 10^{21}$	24×10^{21}
Maximum pellet frequency [Hz]	60	15
Pellet velocity [m/s]	50 - 200	100 - 500

The HFPI is connected to the vacuum vessel via three tracks to different pellet injection locations and directions. As shown in figure 1 these are a) perpendicular injection on the magnetic low field side (LFS), b) oblique injection on the magnetic high field side (HFS) and c) oblique injection on a higher location at the high field, which is called Vertical high field side (VHFS). The velocity of the pellets leaving the injector is measured by a pair of light curtains. Additionally passing time and pellet mass

is evaluated at one or two different positions per injection track employing microwave cavities. Further details on the pellet injection system can be found in [8]

Most experiments reported in this paper have been carried out with the injector in

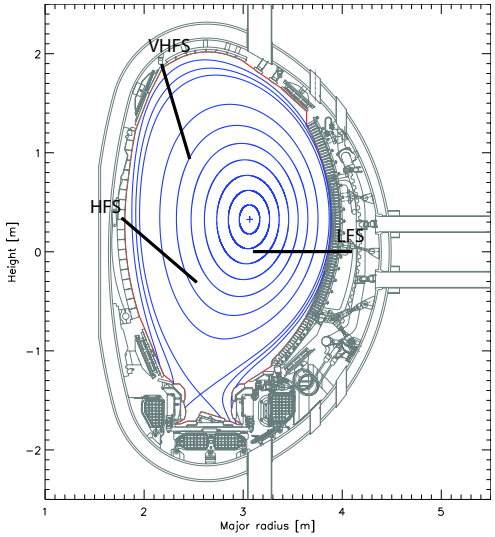

Figure 1. Poloidal cross section of JET with flux surfaces for a typical x-point plasma (blue) and pellet Injection locations and directions (black).

the plasma fueling mode hence with relatively large pellets ($2.2 - 2.4 \times 10^{21} D$). These have been injected exclusively from the magnetic low field side. Discharge 78606 is an exception, during which the injector has been operated in the pacing mode producing relatively small pellets. These have been guided to the VHFS.

Table 3 displays an overview of some pellet parameters for the discharges analyzed in this paper. The abbreviations in table 3 mean (#) number of the discharge, (Type) mode of injector operation, (Location) pellet injection location, (l_{pel}) nominal length of the pellet, (N_{pel}) nominal number of atoms per pellet, (f_{pel}) pellet frequency and (v_{pel}) average pellet velocity measured by the pair of light curtains subsequent to the injector exit.

Table 3. Overview of pellet parameters of the discharges analyzed in this paper

#	Type	Location	l_{pel} [mm]	N_{pel} [10^{21}]	f_{pel} [Hz]	v_{pel} [m/s]
76697	Fueling	LFS	3	2.4	10.0	185
77420	Fueling	LFS	4	3.2	3.0 / 2.0	160
77695	Fueling	LFS	3	2.4	5.0	185
78606	Pacing	VHFS	1.6	0.1	20.0	170
79573	Fueling	LFS	2.8	2.2	4.0	190

2.3. Divertor IR Thermography

A new infrared camera viewing the divertor has been installed in JET [9]. The obtained surface temperatures are routinely converted into power flux densities employing the code Theodor [10]. The camera has a maximum frame rate of 28kHz, while for this analysis mainly 11kHz has been used. Integration times between $30\mu s$ and $75\mu s$ have been used. It views from the top of the machine the load bearing septum replacement plate of the outer divertor with a mean spatial resolution of 1.7mm. Also the vertical inner divertor is diagnosed, however only a part of the main deposition area is in the field of view with a spatial resolution of 5.2mm. Due to this only data from the outer divertor have been used for the analysis presented here.

2.4. Analysis methods

Information on the evolution of ELM events can be gained from the signal of the power deposited on the inner and outer divertor ($P_{div,in}$ and $P_{div,out}$). As high quality data of the divertor power is restricted to the outer divertor, we use $P_{div,out}$ for the ELM recognition. Figure 2 shows the evolution of $P_{div,out}$ for a typical spontaneous ELM together with other signals from fast sampling diagnostics commonly used for ELM analysis. Main characteristic features are the steep rise within a few hundreds of μs and the decay, which transmutes into a close to exponential type decay.

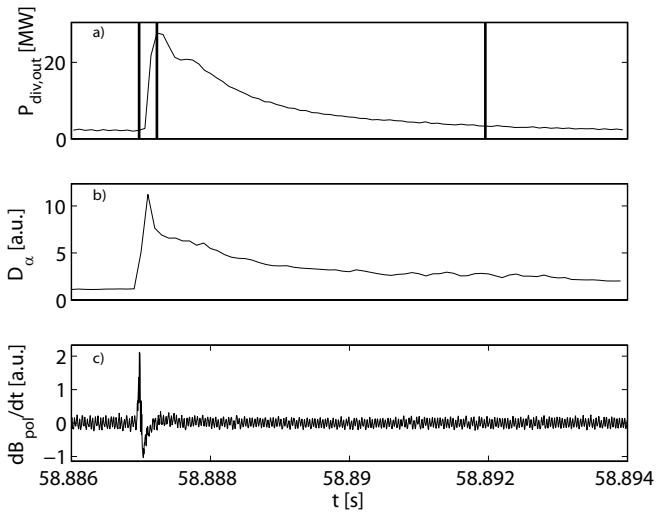

Figure 2. Characteristic evolution during an ELM of a) power deposited on the outer divertor b) divertor D_α-radiation c) time derivative of the poloidal magnetic field measured on the outer mid plane. Vertical lines in the upper plot indicate from right to left $t_{ELM,start}$, $t_{ELM,max}$ and $t_{ELM,end}$

In order to allow systematic data analysis time markers $t_{ELM,start}$, $t_{ELM,max}$ and $t_{ELM,end}$ for onset, peak and final stage of all ELMs are calculated. The standard

algorithm for that identifies $t_{ELM,start}$ with the time, when a certain threshold is exceeded by $\partial P_{div,out}/\partial t$, while $t_{ELM,max}$ is the time, where $P_{div,out}$ has its maximum value within a certain time interval. $t_{ELM,end}$ is defined as the time, where the maximum power flux density has its characteristic minimum after the ELM, with an upper limit of $t_{ELM,start}$+5ms.

Generally only ELMs appearing more than a certain arbitrarily chosen threshold duration ($\sim 10ms$) after the previous ELM have been considered to ensure a minimum in comparability of pedestal conditions. For the classification of an ELM as a pellet induced ELM different criteria sets had to be chosen for fueling type and pacing type pellets. For fueling type pellets two criteria have to be met simultaneously. Firstly the time between pellet detection by a microwave cavity in the flight tube and ELM detection in the plasma as described above has to correspond to the pellet velocity measured by the light curtains within tolerance. Secondly correlated in time a rapid increase of the density (density jump) integrated with the interferometer along a line of sight intersecting only with the plasma edge has to be observed.

For pacing type pellets the standard resolution of the interferometry system does not allow to observe a density jump. Therefore the pellet D_α-monitor, which is only reliable for the VHFS, has been used. The ablation cloud appears in the view of the diode producing the pellet D_α-monitor just prior to reaching the last closed flux surface [11]. We categorized ELMs as pellet induced ELMs when appearing with an unambiguous temporal correlation to a peak on this D_α-monitor exceeding a given threshold.

For discharges 76697 resp. 79573 the ELM selection criteria as explained above have been applied with a minimal duration between ELMs of 10ms giving 19 resp. 12 pellet induced ELMs and 23 resp. 199 spontaneous type I ELMs. Figure 3 shows the detected ELMs for discharge 76697 in conjunction with the signal of $P_{div,out}$. Spontaneous and pellet induced ELMs appear here as interleaved sets.

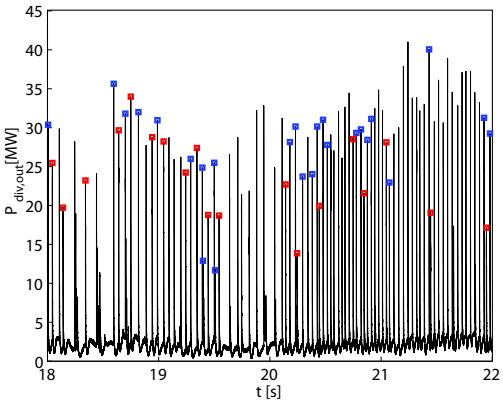

Figure 3. JET Discharge 76697 (Fueling size pellets / LFS): Power to the outer divertor: The squares mark the analyzed spontaneous (blue) and pellet induced (red) ELMs.

3. Evolution of a typical pellet induced ELM

In order to characterize the evolution of a pellet induced ELM we first estimate the location of the pellet at several instances during the flight of the pellet through the plasma edge. We employ ablation modeling with the code HPI2 [12] in combination with data from interferometry with high temporal resolution.
HPI2 determines the pellet particle source by application of a pellet ablation model, which is based on the neutral gas and plasmoid shielding description. For completeness the reader should note that ExB-drift, pre-cooling and acceleration due to inhomogeneous ablation has not been considered for the simulation reported here. As experimental reference a pellet injected at 18.76s in discharge 79573 has been used. Ablation modeling input data are pellet parameters (size, velocity) as well as the last density and temperature profiles before the investigated ELM acquired by the High Resolution Thompson System and equilibrium data calculated by EFIT.
Figure 4 shows the evolution of power to the outer divertor target, signal from a Mirnov coil, line integrated density and modeled ablation rate. We assume, that about at the time of the onset of the pellet ablation (1) the pellet crosses the equilibrium separatrix. At the onset of the ELM signature on the magnetic signal (2) the pellet has moved from the separatrix 5 to 6cm along its trajectory to a location well inside the pedestal top. The evolution of the line integrated density and the modeled ablation rate suggests that about $200\mu s$ later the pellet is estimated to be fully ablated (4).
The onset (3) respectively the end of the rise phase (5) of the ELM associated power flux to the outer divertor is observed $80\mu s$ respectively $500\mu s$ after the onset of the ELM signature on the magnetic signal. For comparison we consider the pedestal top temperature of around 1keV measured by ECE and assuming equality of electron and ion temperature (supported by Charge Exchange Recombination Spectroscopy data) we derive an ion sound speed of 310km/s. Thus a free streaming thermal ion would travel the connection length from outer mid plane to the outer divertor target ($\sim$29m) in about $90\mu s$.

4. Comparison of thermal energy losses and radiated energy

Table 4 summarizes energies transferred between $t_{ELM,start}$ and $t_{ELM,end}$ averaged over the corresponding set of ELMs for discharges 76697, 78606 and 79573. The abbreviations mean (#) number of the discharge, (Δt) time interval of flat top phase used for data analysis, (Group) spontaneous respectively pellet induced ELM, (Number) number of ELMs in this subset, ($\Delta W_{in,nbi,rel}$) relative integrated input power form neutral beam heating, ($\Delta W_{dia,rel}$) relative drop of plasma stored energy obtained by measurement with a diamagnetic loop, ($\Delta W_{mhd,rel}$) relative drop of plasma stored energy acquired via integration of the pressure profile from obtained by equilibrium reconstruction code EFIT and ($\Delta W_{rad,rel}$) relative total radiated energy from bolometry data (temporal

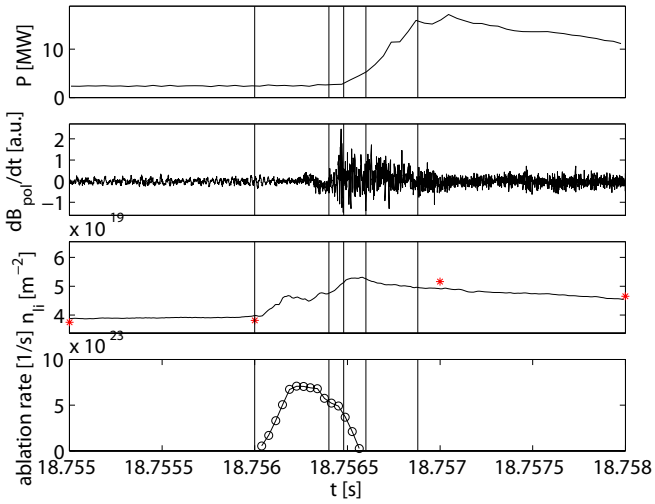

Figure 4. Evolution of power to the outer divertor target, signal from a Mirnov coil, line integrated density (standard: stars, high temporal resolution: full line) and modeled ablation rate during a pellet induced ELM in discharge 79573 (Fueling size pellets / LFS). Ablation rate has been allocated in time using the pellet velocity measured by the microwave cavities and assuming a coincident onset of ablation and fast density increase. Vertical time marks in chronological order refer to: 1) start of ablation, 2) onset of ELM signature on the magnetic signal, 3) onset of increased power flux to the outer divertor, 4) end of ablation, 5) end of the rise phase of the power flux to the outer divertor.

resolution: 0.2ms), where 'relative' stands for 'relative to the stored energy W_{mhd} at $t_{ELM,start}$'.

In view of an estimate of the ELM associated energy deposited on the plasma fac-

Table 4. Comparison of averaged energies transferred during ELMs for spontaneous (S-ELM) and pellet induced ELMs (P-ELM) in the discharges 76697 and 79573: For 79573 the ELM associated drop ΔW_{dia} is masked by a different effect for a significant part of the analyzed time interval.

#	Δt [s]	Group	Number [1]	$\Delta W_{in,nbi,rel}$ [%]	$\Delta W_{dia,rel}$ [%]	$\Delta W_{mhd,rel}$ [%]	$\Delta W_{rad,rel}$ [%]
76697	18-22	S-ELM	23	1.4 ± 0.1	2.9 ± 1.2	2.8 ± 0.9	2.1 ± 0.3
		P-ELM	19	1.3 ± 0.1	5.8 ± 1.3	4.6 ± 0.8	4.1 ± 0.6
79573	14-21	S-ELM	199	1.2 ± 0.3	-	2.6 ± 1.0	1.2 ± 0.4
		P-ELM	12	1.6 ± 0.3	-	4.1 ± 1.4	2.2 ± 0.7
78606	16-22	S-ELM	74	1.2 ± 0.0	5.6 ± 0.9	7.1 ± 0.5	2.8 ± 0.6
		P-ELM	7	1.2 ± 0.1	4.9 ± 0.9	6.5 ± 0.8	2.3 ± 0.5

ing components we consider here losses of plasma stored energy, radiated energy and heating energy. The later one in all analyzed discharges is comparable for both ELM categories. In comparison in both discharges with fueling size pellets (76697, 79573) on average 60-70% higher losses of the absolute thermal energy are found for pellet induced ELMs compared to spontaneous ELMs. As an example figure 5 shows the drop of W_{mhd}

for spontaneous and pellet induced ELMs in discharge 79573. In the displayed time window the spontaneous ELMs are interlaced by three pellet induced ELM. One can clearly see that the drops of W_{mhd} associated with the first and the third of these belong to the lagest drops of all ELMs in this period. Even the second pellet induced ELM shown, which is observed in relation very early after the predecessing ELM, has a drop of stored energy, which is about average for this time window.

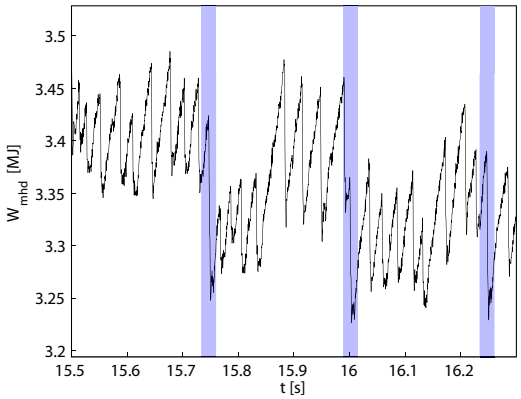

Figure 5. Evolution of W_{mhd} during a time interval with spontaneous and pellet induced ELMs in discharge 79573 (Fueling size pellets / LFS). Times at which pellets have been injected are indicated by blue boxes.

The question is raised, if ELMs induced by pellets of arbitrary mass (fueling and pacing type) are associated with a larger drop of plasma stored energy in comparison to spontaneous ELMs. The data situation did not allow a direct comparison of fueling and pacing type pellets. To get some indication on the pellet mass dependence of the drop in plasma stored energy for each analyzed pellet induced ELM the associated density jump has been taken as a measure for the size of the pellet entering the plasma. Figure 6 shows the dependence of stored energy (a), radiated energy and ELM rise time (c) on this pellet size measure for discharge 76697. In particular figure 6a) shows the dependence of ΔW_{mhd} and ΔW_{rad}. For a variation of the density jump by a factor of 5 only a weak scaling of ΔW_{mhd} has been found. The extrapolation of the linear fit to zero density increment is clearly above the values for spontaneous ELMs (full squares). For completeness should be added that a scaling with the time elapsed since the previous ELM has not been found for any of the quantities plotted in figure 6.

Another indication gives discharge 78606 with pacing type pellets injected via the VHFS track. In this case the drop in plasma stored energy associated with the ELM has on average a similar extent for both categories of ELMs. It is however not clear, if ELMs induced by pellets injected from the VHFS are fully comparable to ELMs induced by pellets injected from the LFS.

The energy ΔW_{rad} radiated between $t_{ELM,start}$ and $t_{ELM,end}$ constitutes a significant part of the thermal energy losses during the ELM. Comparing spontaneous with pellet

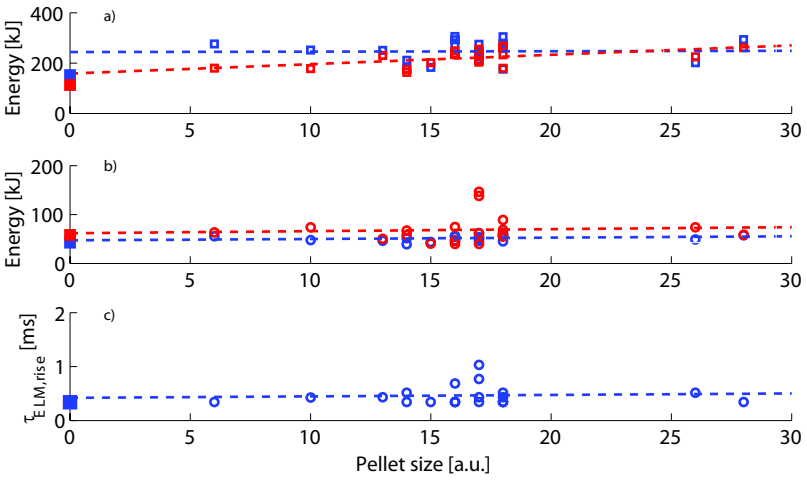

Figure 6. Pellet size dependence of various quantities for pellet induced ELMs in discharge 76697 (Fueling size pellets / LFS): a) ΔW_{mhd} (blue) and ΔW_{rad} (red) b) $W_{div,out}$ (blue) and $10 \times W_{div,out,rise}$ (red) c) $t_{ELM,max} - t_{ELM,start}$. Dashed lines indicate linear regressions, full squares represent respective mean values of spontaneous ELMs. $W_{div,out,rise}$ is the energy deposited on the outer target during ELM rise phase

.

induced ELMs we see for ΔW_{rad} a similar behavior as for the losses in plasma stored energy. For ELMs induced by fueling type pellets ΔW_{rad} is twice as high as for spontaneous ELMs. Figure 6a) indicates a slight increase of ΔW_{rad} with pellet size. A plausible explanation of this could be that the plasma edge is cooled by the pellet material leading to a lower fraction of fully ionized particles and increased line radiation. This is consistent with the observation that ELMs induced by pacing type pellets are associated with comparable radiated energies as spontaneous ELMs.
The total energy flux towards all plasma facing components can be expressed as $\Delta W_{dia} + \Delta W_{in,nbi} - \Delta W_{rad}$ respectively $\Delta W_{mhd} + \Delta W_{in,nbi} - \Delta W_{rad}$. In summary this quantity is similar for spontaneous ELMs and ELMs induced by both fueling and pacing type pellets.

5. Analysis of toroidal asymmetry of divertor deposition and SOL heat flux of pellet induced ELMs

Pellet injection is done at a fixed toroidal position. This raises the question, if the spatial structure of the perturbation and the heat transport associated with pellet induced ELMs features a corresponding toroidal asymmetry. Divertor infrared thermography

as well is carried out at a certain toroidal position [9]. Thus the best approach to investigate such an asymmetry would be to carry out measurements at various toroidal locations. As this has been outside the diagnostic capability of JET †, as an alternative a scan of the toroidal magnetic field at constant plasma current has been developed and carried out. The comparability between the ELMs appearing during this scan is reduced due to changes of the background plasma due to variation of the toroidal magnetic field. For instance the frequency of the spontaneous ELMs increases with rising absolute value of $|B_T|$.

5.1. Results obtained by Divertor IR Thermography

Figure 7 shows the evolution of the power flux density on the outer divertor for a period of 25ms during JET discharge 79573. Three ELM events take place within this time interval at 20.7376s, 20.7487s and 20.7586s. The first and the last ELMs are spontaneous, while the middle one is pellet induced. Between the ELMs the peak deposition can be located at 2.72m to 2.74m (inter-ELM strike line). For all three ELMs there is a peak of power flux density at the inter-ELM strike line or at slightly higher radii. For the pellet induced ELM additionally a power flux density peak with higher amplitude can be observed at 2.80m. Deposition of this extent in a location so far from the inter-ELM strike line has not been observed with the employed divertor IR diagnostic at JET for spontaneous ELMs. This behavior has to be distinguished from the ELM associated strike point movements reported in [13], as there is still significant deposition near the inter-ELM strike line for the pellet induced ELM.

Figure 8 shows the evolution of power flux profiles for both categories of ELMs during

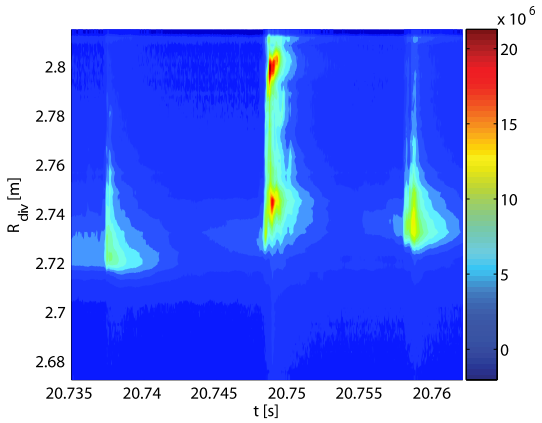

Figure 7. Power flux density $[W/m^2]$ on the outer divertor during JET discharge 79573 (Fueling size pellets / LFS) as a function of time and major radius

† In 2011 two additional divertor IR cameras come into operation at JET. One of them views the outer divertor target in an identical way as the existing camera but at a different toroidal location. The other one is guided towards the inner divertor target.

the scan of absolute value of the toroidal magnetic field from lower to higher absolute values. Each line represents the power flux density profile of an individual ELM. The power flux densities are averaged in time from the time of the peak power deposition for 0.4ms. The set of analyzed pellet induced ELMs includes all ELMs during the B_T-ramp fulfilling the selection criteria described in 2.4.

The profiles for the spontaneous ELMs preceding the pellet induced ELMs (figure 8a) all have one main peak with a steep shoulder towards the private flux region and a flat shoulder towards the far SOL. The radial location of the peak does not significantly change with $|B_T|$ and lies close to the pre-ELM power flux density maximum. Profiles for other spontaneous ELMs (e.g. the ELMs succeeding the pellet induced ELMs) are identical and not shown here. In clear contrast, the profiles for pellet induced ELMs (figure 8b) have peaks at a variety of locations changing with $|B_T|$. For most pellet induced ELMs one can interpret the shape of the profile as the superposition of a profile that is similar to that of a spontaneous ELM and an additional dominant peak. Staying in this interpretation the ratio between the intensity of the two components changes clearly between different pellet induced ELMs. We identify a trend of such pellet induced additional peaks moving outwards with $|B_T|$.

In order to verify the radial movement of the pellet induced peak power flux density

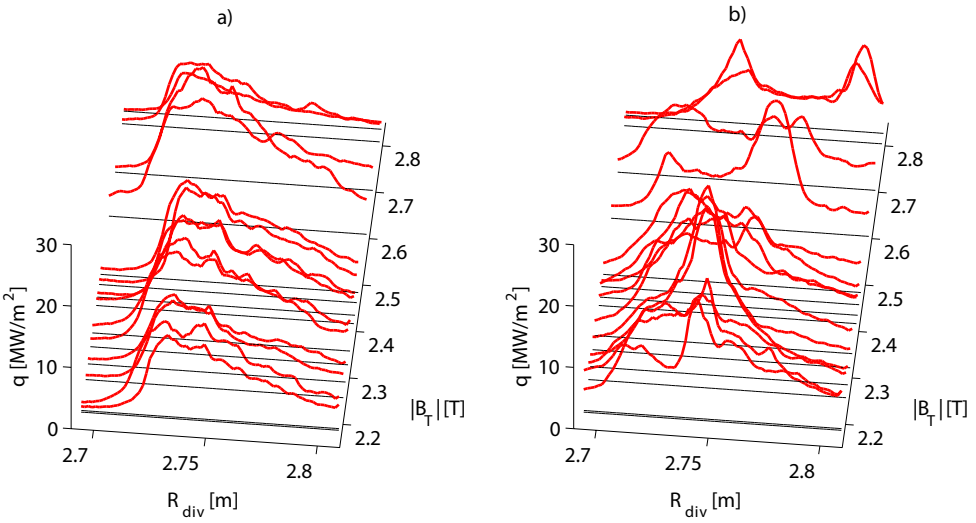

Figure 8. Deposition profiles of individual ELMs on the outer target in discharge 79573 (Fueling size pellets / LFS) as a function of $|B_T|$: a) ELMs directly preceding pellet induced ELMs and b) pellet induced ELMs. Each profile shows the spatial dependence of the power flux densities averaged from t=0 to t=0.4ms with t=0 defined by the peak power deposition. Horizontal lines are to support the allocation with $|B_T|$.

due to the change of the toroidal magnetic field an experiment with a scan of $|B_T|$ in the opposite direction (from higher to lower absolute values) has been carried out in

JET discharge 77695. Figure 9 shows the evolution of the deposition profiles for pellet induced ELMs on the outer target. It has to be noted that for this discharge the divertor has been contaminated with a deposition layer around a radial location of 2.74. Due to this the calculated power flux values are artificially enhanced at this location as it can be seen for the spontaneous ELMs. Taking this into account still a trend of peaks located at higher radii for higher $|B_T|$ can be observed.

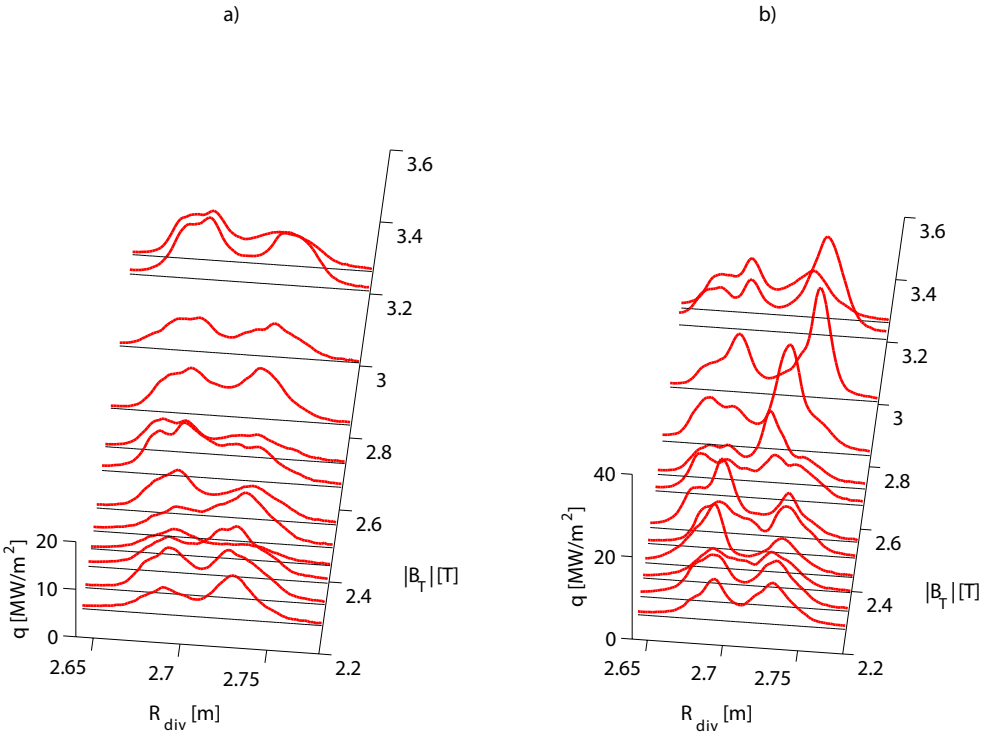

Figure 9. Deposition profiles of individual ELMs on the outer target in discharge 77695 (Fueling size pellets / LFS) as a function of $|B_T|$: a) ELMs directly preceding pellet induced ELMs and b) pellet induced ELMs. Each profile shows the spatial dependence of the power flux densities averaged from t=0 to t=0.4ms with t=0 defined by the peak power deposition. Horizontal lines are to support the allocation with $|B_T|$.

5.2. SOL Field line Tracing

In order to investigate the question of the origin of the $|B_T|$-dependent location of peaks observed exclusively in conjunction with pellet induced ELMs SOL field line tracing has been employed. We traced field lines starting from the outer mid plane (MP) at fixed vertical and toroidal coordinates Z_{mp} and Φ_{mp} corresponding to the pellet injection location (Z_{pel} and Φ_{pel}) and variable radial coordinate R_{mp} such that the start point is located in the SOL. Magnetic field lines obtained via the equilibrium reconstruction code EFIT have been followed from (R_{mp}, Z_{mp}, Φ_{mp}) until they hit the outer divertor target defining the coordinates (R_{div}, Z_{div}, Φ_{div}). In such a mapping of equilibrium 3D

SOL field lines both R_{div} and Φ_{div} are functions of R_{mp} as can be seen in figure 10. Consequently the target end points of this field lines for a continuous variation of R_{mp} build a spiral-like structure on the outer target [14, 15]. Changing $|B_T|$ at constant plasma current approximately corresponds to a rotation of this spiral-like structure as can be seen from the relative vertical shift between curves for different values of $|B_T|$ in figure 10b. Thus a variation of $|B_T|$ leads to a radial movement of the intersection $R_{div,flt}$ of the spiral-like structure with the toroidally localised IR observation area.

Figure 11 shows the radial target position of the largest peaks of the divertor heat

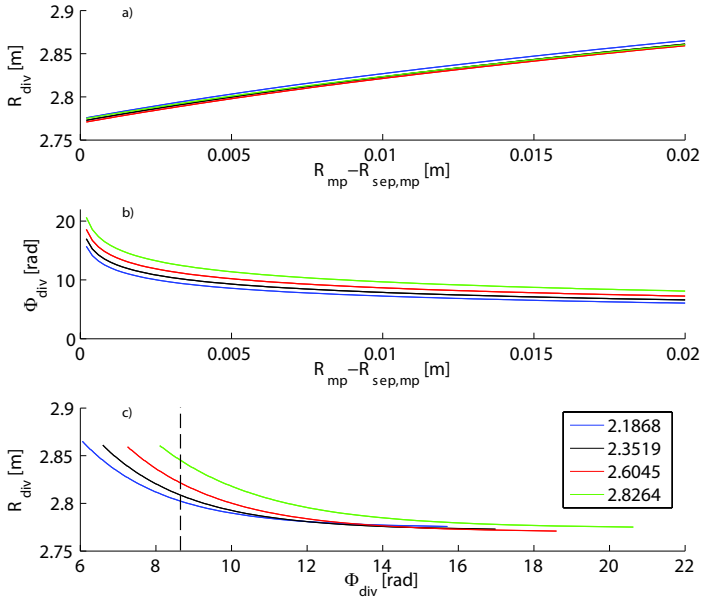

Figure 10. Basic relations of field line tracing: a) R_{div} and b) Φ_{div} as functions of $R_{mp} - R_{sep,mp}$ and c) R_{div} as function of Φ_{div} for 4 different absolute values of the toroidal magnetic field in T indicated by the color code. The variation of the range of the values for R_{mp} is due to the change in the position of the separatrix in the equilibrium reconstruction over time. Vertical dashed line indicates the position of the camera.

flux deposition profiles defined by a threshold criterion versus $|B_T|$. The threshold criterion is fulfilled when the local power flux density exceeds 85% of the maximum power flux density within the profile during an investigated period (t=0 to t=0.4ms with t=0 defined by the peak power deposition). Again the difference in the distribution of locations of peak power flux densities for spontaneous and pellet induced ELMs is clearly visible. In particular one can see that the locations of most peaks associated with the later ones show a clear dependence on $|B_T|$. For completeness we add that a radial motion of the position of a peak during an ELM has not been observed.

In order to compare the experimental peak locations with predictions from magnetic field line tracing we vary R_{mp} until approaching with Φ_{div} the toroidal position of the IR divertor observation. For the analyzed set of pellet induced ELMs the difference

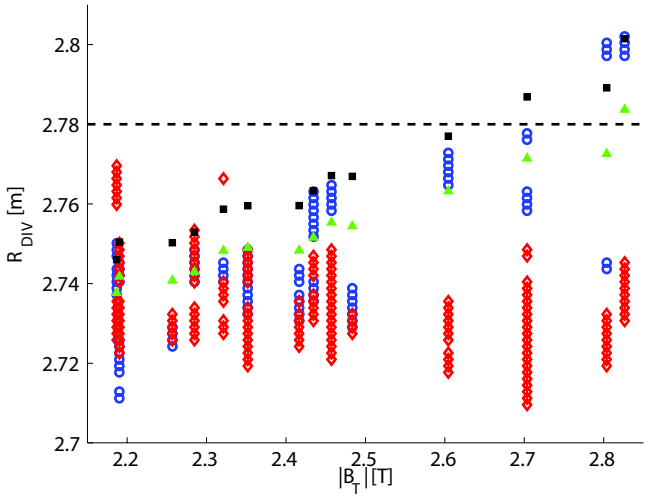

Figure 11. Experimentally observed peak positions (criterion is described in the text) for pellet induced ELMs (blue dots) and spontaneous ELMs (red dots) as function of $|B_T|$ in discharge 79573 (Fueling size pellets / LFS): Squares indicate predicted and corrected peak positions ($R_{div,flt,corr} = R_{div,flt} + \Delta R$, where $\Delta R = R_{div,sep,ir} - R_{div,sep,flt}$) on the basis of field line tracing with $\Phi_{mp} = \Phi_{pel}$ (black) respectively $\Phi_{mp} = \Phi_{pel} + \pi/4$ (green). Horizontal dashed line indicates radial position of triple Langmuir probe 24.

between the values of R_{mp} after this optimization and the radial position of the strike line mapped to the mid plane varies between 0.5 and 1.5cm.

Due to imperfections of the equilibrium reconstruction the absolute position of the strike line $R_{div,sep,flt}$ and of the inter-ELM strike line measured with the divertor IR system $R_{div,sep,ir}$ can differ significantly, in particular in high heated H-mode plasmas. We correct $R_{div,flt}$ to $R_{div,flt,corr} = R_{div,flt} + \Delta R$, where ΔR equals $R_{div,sep,ir} - R_{div,sep,flt}$. The values of $R_{div,flt,corr}$ describing the corrected expected radial peak location at the toroidal location of the IR observation based on field line tracing, are also plotted in figure 11. One can see that the prediction is in very good agreement with the experimental observation for the pellet induced ELMs with a slight systematic deviation towards higher radii.

In figure 11 the predicted peak locations for field lines starting with an offset ($\Phi_{mp} = \Phi_{pel} + \pi/4$) are also shown (green squares). One can see that the experimentally observed peak locations to a good extent are located between the predicted peak locations for $0 \leq \Phi_{mp} - \Phi_{pel} \leq \pi/4$. The fact that the predicted peak locations for $\Phi_{mp} = \Phi_{pel}$ do not exactly agree with the measured could be explained by effects of toroidal plasma rotation. For simplicity we assume that the ablated pellet material, which is leading to a high pressure in the vicinity, without any delay picks up the toroidal rotation frequency $f_{rot,tor}$ of the background plasma and rotates with this for a time interval τ_{ej}, until a part of this material crosses the separatrix and follows the field line as described above. We estimate the product of the two quantities mentioned: $f_{rot,tor} \times \tau_{ej} \leq 1/8$

From Edge Charge Exchange Recombination Spectroscopy we determine an average toroidal rotation frequency of about 6kHz for the location of the pedestal top for times between 55s and 60s. Inserting this value in the inequality gives $\tau_{ej} < 20\mu s$. Considering lower rotation frequencies for locations further outside (e.g. in the middle of the steep gradient region) would lead to an increase of this number. Also accounting for a realistic toroidal acceleration of the pellet material would increase this duration. In any case it is remarkable that the ELM associated ejection of pellet material happens on such a fast time scale. This estimation is of the same order of magnitude as the one carried out in [16]. Here the time between the pellet reaching the triggering location and the onset of magnetic fluctuations associated with the ELM observed by Mirnov coils has been estimated to be $50\mu s$.

5.3. Correlation with data from divertor Langmuir probes

Triple Langmuir probes are routinely employed to measure particle fluxes and electron temperatures in the JET divertor [17]. The system has a temporal resolution of 0.1ms and a radial resolution of ∼1cm. We used triple probe 24, which is measuring the ion saturation current at a pin located in a toroidal distance of ∼ 26° from the IR observation location.

Figure 12 shows the ion saturation current from triple Langmuir probe 24 and the

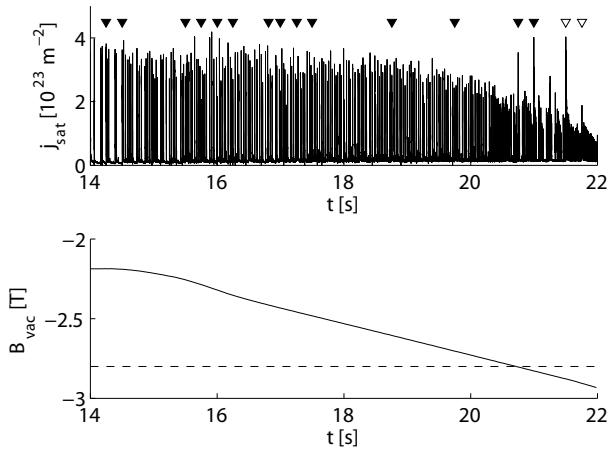

Figure 12. Ion saturation current from triple Langmuir probe 24 and vacuum magnetic field on magnetic axis for discharge 79573 (Fueling size pellets / LFS). Triangles indicate time of analyzed pellet induced ELMs (filled) and additional (open) pellet induced ELMs (open). Vertical line indicates $|B_T| = 2.8T$

vacuum magnetic field on the magnetic axis during the toroidal magnetic field ramp as well as times, at which pellet induced ELMs are identified. It can be seen that the ELM related peaks of the ion saturation current are of similar extent for spontaneous and pellet induced ELMs for absolute values of the toroidal magnetic fields lower than 2.8T. For higher values one can clearly see that the peaks correlated with the pellet induced

ELMs are up to two times higher than the adjacent peaks of spontaneous ELMs.
Triple Langmuir probe 24 is measuring at a radius of 2.78m as indicated as dashed line in figure 11. The ion saturation current is proportional to the particle flux to the divertor. We assume that a part of the SOL transport associated with pellet induced ELMs is following the trajectory as described in 5.2. Hence a part of the divertor deposition on the outer divertor would have the described spiral-like structure. Consistently this spiral intersects the toroidal location of the employed Langmuir probe for lower absolute values of the toroidal magnetic field at radii lower than 2.78m. Only for $|B_T|$ higher than 2.8T (figure 11) the additional contribution from this transport specific to pellet induced ELMs is observable with this diagnostic. The peak particle flux associated with spontaneous ELMs is decreasing with rising absolute values of B_T, while this is not the case for pellet induced ELMs.

5.4. Code predictions from JOREK

The non-linear MHD code JOREK [18] evolves a set of reduced MHD equations in toroidal geometry. The poloidal plane is discretised using cubic Bezier finite elements [19] while the toroidal variation is described by a Fourier series. The computational domain includes the plasma center, the separatrix and x-point and the open field lines in the SOL. Non-linear MHD simulations of ELMs with the JOREK code have shown good qualitative agreement with respect to features such as the formation of filaments and the fine structure in the energy convected to the target [18].
For the simulation of pellet induced ELMs a JET-like H-mode plasma [20] has been chosen with an pedestal pressure gradient such that it is marginally stable with respect to low to medium-n ballooning modes. In the simulations the pellet is described by a large local particle source located in the middle of the pedestal with a half-width of 2 cm and acting adiabatically on the plasma.
Figure 13a) shows a contour of the density $\sim 50\mu s$ (for a central density of $5 \times 10^{19} m^{-3}$) after the start of the pellet source. Also shown is the temperature on the separatrix and the heat flux convected to the target. The dominant toroidal mode number of this helical perturbation is n=1. At this time the pressure in the pellet cloud at the mid plane is about twice the pressure at the top of the pedestal and remains relatively constant. Figure 13b) shows a closer view of the density profile at the toroidal angle where the pellet cloud is passing the x-point. Here as well the contours of the electrostatic potential (ExB flow lines) from the JOREK calculation are illustrated. From the high density region of the helical pellet cloud there is an ExB flow across the separatrix close to the x-point directed towards the divertor. This ExB flow is clearly stronger towards the outer divertor leg, which is the one with the higher power flux densities simulated on the divertor.
The ExB flow leads to prompt losses of the density close to the x-point. Since the particles crossing the separatrix have been heated by parallel transport inside the

separatrix, there is also an associated convected heat transport. After the separatrix crossing the parallel transport might have a more dominant role.

Figure 14a) illustrates the power flux density on the outer divertor calculated by

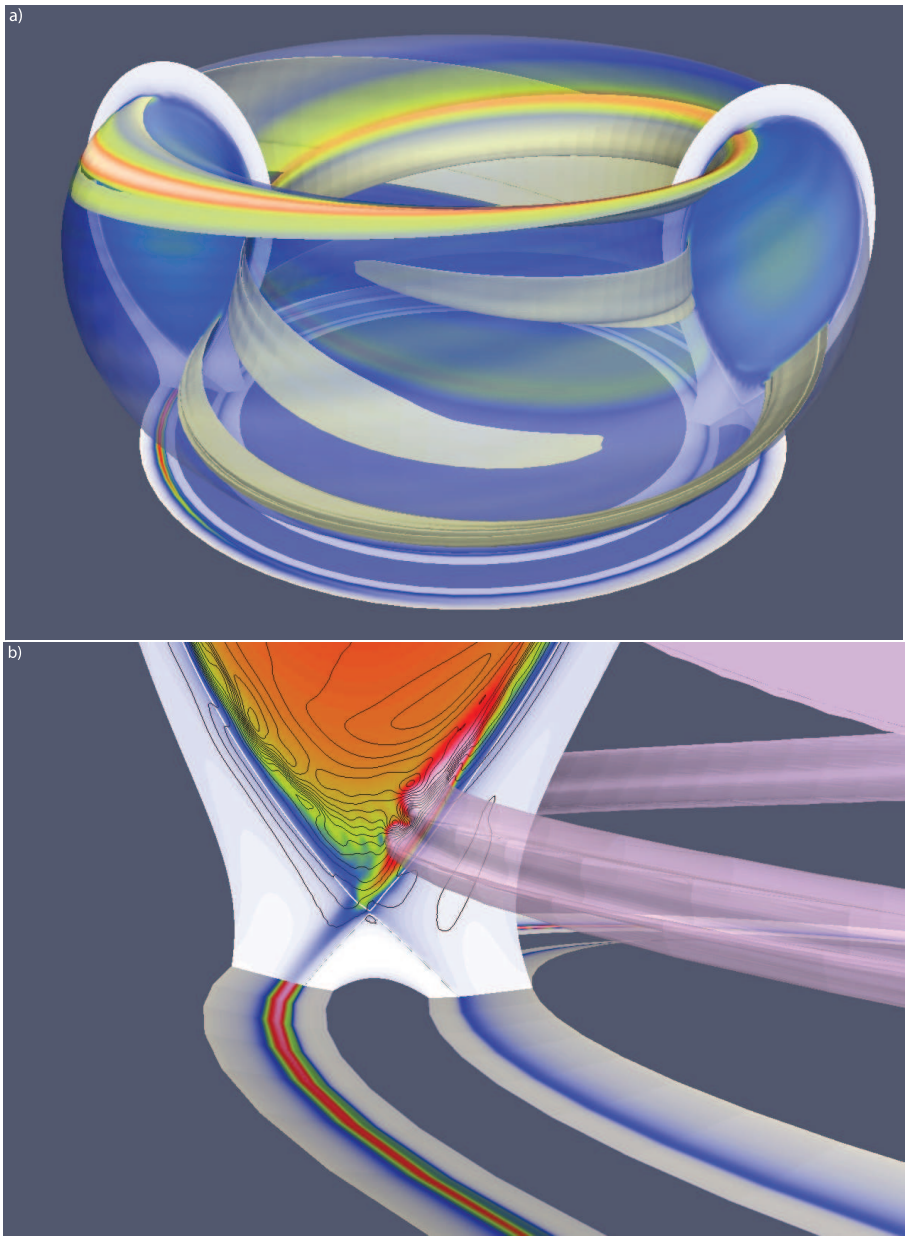

Figure 13. a) The density contour ($n = 1.1 \times n_{mag.axis}$) at $t \sim 50\mu s$, the temperature at the separatrix (red-blue scale) and the convected heat flux to the target. The pellet injection location is on the LFS mid plane on the side of the plasma, which is turned away from the viewer. b) Close-up of the density profile together with the contours of the electrostatic potential (ExB flow lines, black contours). The lower part shows the heat convected to the target.

JOREK for a time $\sim 40\mu s$ after the onset of the particle source as a function of radial divertor position R_{div} and toroidal angle Φ. At a radial position of 3.25m there is high or even maximum deposition for all toroidal angles. This position corresponds to the

separatrix mapped on the outer divertor target. In addition to this symmetric deposition component another component changing maximum power flux density and profile shape with the toroidal angle can be observed. This component is spreading toroidally towards a symmetric shape with approximately the local sound speed in the x-point region.

In order to isolate the asymmetric component we identify the toroidal angle, for which

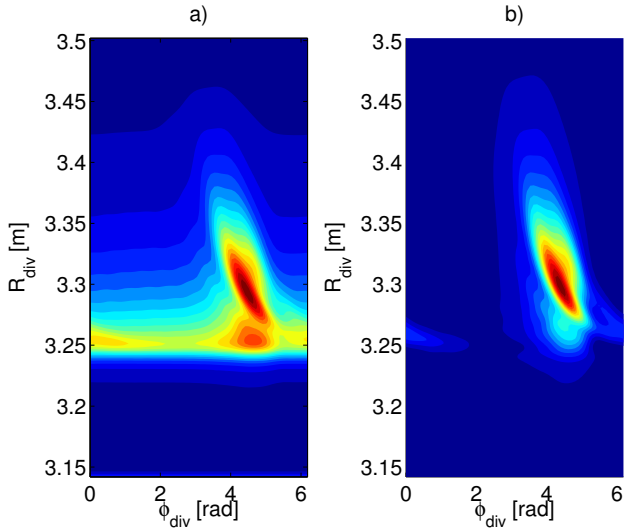

Figure 14. Heat flux density on the outer divertor target from JOREK simulation: a) Total deposition b) Asymmetric component. The pellet injection location is at $\Phi = 0$. Note that the JOREK calculations have been carried out on the basis of a tokamak slightly larger than JET.

the power flux density integrated along the radial direction is minimum. We select the radial power flux density profile for this toroidal angle as the profile, which describes in the best way the symmetric component. This profile is similar to the toroidaly averaged profile for the time t=250, at which the toroidal variation of the radially integrated power flux density is at a level of 0.2%. We subtract this profile representing the symmetric component of the radial power flux density profiles for each toroidal angle and obtain the profiles of the asymmetric component, which are shown in figure 14b).

Figure 15a) shows the maximum power flux density of the total deposition and the asymmetric component as a function of the toroidal angle. The maximum variation of this value for the total deposition is 66% of the mean value. Thus a considerable toroidal asymmetry in the maximum power flux density is predicted by JOREK. Figure 15b) indicates the location of the maximum power flux density for all toroidal locations for the total deposition and the asymmetric component. In real space coordinates the line for the total deposition would appear as a structure similar to a spiral. The relation between toroidal angle and radial divertor location, which it describes, is clearly reminiscent of the relation between the same coordinates for the target points obtained by magnetic field line tracing as described above (figure 10c).

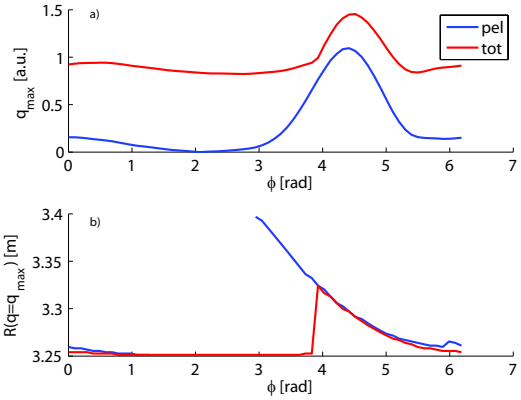

Figure 15. Maximum power flux density (a) and radial location of the maximum power flux density (b) as a function toroidal angle: Total deposition (red) and asymmetric component (blue). For the asymmetric component in b) only toroidal locations are regarded, where the maximum heat flux density exceeds 4% of the maximum of the heat flux density for the entire outer divertor.

5.5. Model of the asymmetric component

A number of indications regarding the nature of the toroidally asymmetric component of the divertor deposition associated with pellet induced ELMs has been gathered. JOREK pellet simulations have given evidence of a transport path crossing the separatrix in the x-point region. As well they have found asymmetric deposition on the outer divertor. However it is not clear that, in the simulations, the prompt density losses at the x-point are directly related to the onset of a pellet induced MHD instability (ELM).
In JOREK simulations in circular geometry, which can be identified as pellet induced ELMs, the flow at the separatrix has large radial components especially in the vicinity of the pellet injection location. These flows are driven by the ballooning instability that is destabilized by the high pressure observed in JOREK and that develops due to the heating by parallel conduction of the pellet cloud. The instability driven flow in addition to the usual ExB flows would evoke a strong radial transport at the pellet injection location, which constitutes a second possible transport path across the separatrix.
The SOL field line tracing carried out in this work has been based on this second transport path. The good agreement of the predicted and measured peak locations at the divertor target allow two possibilities. Either there is indeed a dominant component of the SOL transport following the transport path, which is crossing the separatrix in the vicinity of the pellet injection location. If this is not true the asymmetric component is mainly originating from the transport path via the x-point. In this case the divertor deposition structure associated with both transport paths must be very similar.
The question, which of these two paths via the separatrix is dominant could be studied in detail on the basis of fueling size pellets injected only a few ms after the previous ELM. In some of these cases there is indication from the magnetic measurements that no MHD-activity is induced. Such a situation might be interpreted as no ELM has been

induced. The main question of such an investigation would be to what extent and with which pattern power is deposited on the divertor during these events.

6. Comparison of ELM divertor heat deposition

In view of the question of ELM affected divertor deterioration it is of high interest to compare various divertor power load aspects for spontaneous and pellet induced ELMs. However as a first step we present a brief comparison of divertor power loads of pellets inducing ELMs in H-mode and pellets not inducing ELMs in L-mode and H-mode.
Figure 16 shows the power deposited on the outer divertor, the divertor D_α-radiation and the line integrated density on edge channel of interferometer for an H-mode phase and a L-mode phase of discharge 77420 and an H-mode phase of discharge 78606. In the H-mode phase of 77420 three density jumps can be identified. These jumps are caused by pellets injected into the plasma, which are marked by vertical lines. At the same time ELM events occur as can be seen from both D_α-radiation and power to the outer divertor. The peak power during these ELMs deposited on the outer divertor is between 10 and 20 MW. During the L-mode phase of this discharge two density jumps of an extent comparable to those during the H-mode phase can identified. However in this cases no correlated increase in the power to outer divertor is observed.

In the case of the H-mode phase in discharge 78606 at 23.38s a pacing size pellet

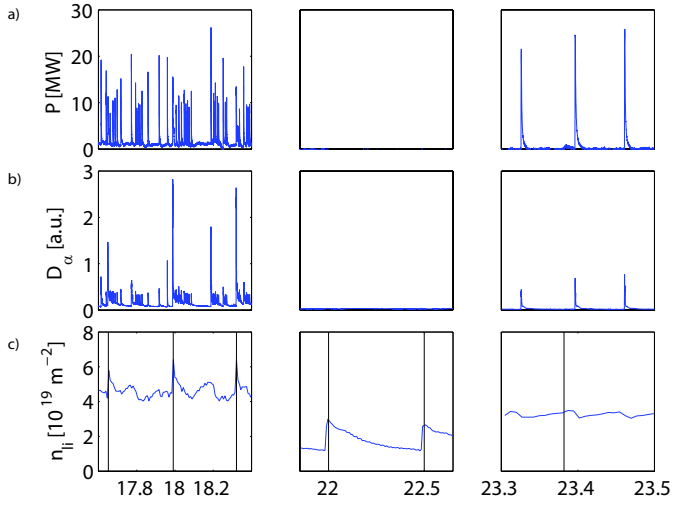

Figure 16. Power deposited on the outer divertor (a), divertor D_α-radiation (b) and line integrated density on edge channel of interferometer (c) for a H-mode phase (left) and a ohmic Phase (middle) of discharge 77420 (Fueling size pellets / LFS) and an H-mode phase (right) of discharge 78606 (Pacing size pellets / VHFS). Vertical lines indicate times of pellets injected into the plasma

is injected leading to a signal on the pellet D_α-monitor (see 2.4) peaks of 1.5V corresponding to 1.5 times the threshold for the categorization as pellet induced ELMs. As can be seen this is not causing any observable increase in both D_α-radiation and power

deposited on the outer target observed by IR thermography. Thus in this case no ELM has been induced by the pellet (For ELMs induced by fueling size pellets this has only been observed, if the time elapsed since the last ELM is less than 4ms.). In summary the only pellet associated case within the cases presented in this subsection with a relevant power flux density is the pellet induced ELM.
In the following we will present a detailed comparison of spontaneous and pellet induced ELMs with respect to several divertor power load aspects. In this context we will consider as well the toroidal asymmetry of the divertor power flux density for pellet induced ELMs.

6.1. Data sets

For this comparative analysis we use the two JET discharges 76697 and 79573. While the first one is carried out under steady conditions, the latter one is associated with a ramp of the toroidal magnetic field. Thus 76697 provides a better basis for a statistical analysis.
Another aspect is related to the question how much the asymmetric profile component is featured at the toroidal position, where the IR observation is carried out. For discharge 79573 this has been exhaustively discussed in section 5. We can conclude from there that the asymmetric component is significant for nearly all pellet induced ELMs in this discharge. Figure 17 shows the profiles of power flux density on the outer divertor for the analyzed pellet induced ELMs and their spontaneous predecessors in discharge 76697 (compare to figure 8). In contrast to discharge 79573 in 76697 no additional peaks are observed in the deposition profiles for the pellet induced ELMs. q_{95} for discharge 76697 is 3.4. In discharge 79573 this value is just outside the scanned interval at the end, where the radial location of the asymmetric component has converged to the strike line position.
Hence we conclude that in discharge 76697 the profiles are recorded at a toroidal location, at which the asymmetric component is minor. Thus we assume that these profiles represent the symmetric deposition component. Summarizing we have the advantageous situation that the observed divertor profile of one of the analyzed discharges (79573) represents the symmetric plus the asymmetric component, while the profile for the other discharge (76697) represents only the symmetric component.

6.2. Comparison of deposition on the outer target

In 4 we have given evidence that the total energy deposited during the ELM on the plasma facing components ($\Delta W_{dia} + \Delta W_{in,nbi} - \Delta W_{rad}$ respectively $\Delta W_{mhd} + \Delta W_{in,nbi} - \Delta W_{rad}$) is similar for spontaneous and pellet induced ELMs. However it is of great interest to compare various deposition characteristics for the well diagnosed outer divertor. The deteriorating effect of ELMs on the divertor targets roughly can be expressed via

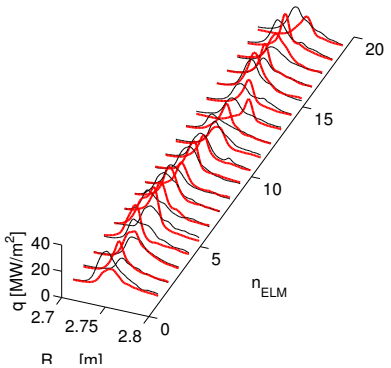

Figure 17. Profiles of power flux density on the outer divertor for the analyzed pellet induced ELMs (red) and their spontaneous predecessors (black) in discharge 76697 (Fueling size pellets / LFS). The power flux density has been averaged between $t_{ELM,max}$ and $0.9 * t_{ELM,max} + 0.1 * t_{ELM,end}$.

the temperature increase ΔT_{ELM} due to a single ELM, which in approximation is a function of thermal material properties $C_{thermal,mater}$, timescales of the ELM rise phase $\tau_{ELM,rise}$, wetted area A_{wet} and the energy $W_{div,rise}$ deposited on the target during the ELM rise phase [4, 6]:

$$\Delta T_{ELM} \approx C_{thermal,mater} \times W_{div,rise}/(A_{wet} \times \sqrt{\tau_{ELM,rise}})$$

Making use of the high spatial resolution of the IR system at the outer target the non material related quantities for this area have been analyzed in further detail. Table 6.2 summarizes these quantities for discharges 76697 and 79573. The abbreviations mean (#) number of the discharge, (Δt) time interval of flat top phase used for data analysis, (Group) spontaneous / pellet induced ELMs, (Number) number of ELMs of this category during investigated period, ($\tau_{ELM,rise}$) duration of the ELM rise phase from $t_{ELM,start}$ to $t_{ELM,max}$, ($A_{wet,rise}$) average wetted area during the ELM rise phase, ($q_{out,max}$) maximum power flux density on the outer target during entire ELM from $t_{ELM,start}$ to $t_{ELM,end}$, ($W_{div,out,rise}$) energy deposited on the outer target during ELM rise phase, ($W_{div,out}$) energy deposited on the outer target during entire ELM. We recommend to compare only values within the same discharge, as the discharges differ in various parameters as partly described above.

Figure 18 shows for the investigated ELMs in discharge 76697 the average evolution of the power deposition on the outer target $P_{div,out}$, which is defined as

$$P_{div,out} = \int_{R_1}^{R_2} q \, \mathrm{d}x \times \pi(R_1 + R_2)$$

, where R_1 resp. R_2 are the smallest resp. highest observed radii and q is the power flux density. Time traces for each ELM have been aligned by $t_{ELM,max}$. Subsequently averages over both categories of ELMs have been taken (coherent ELM averaging). The

Table 5. Non material related quantities determining maximum temperature rise per ELM.

#	Δt [s]	Group	Number [1]	$\tau_{ELM,rise}$ [ms]	$A_{wet,rise}$ $[m^2]$	$q_{out,max}$ $[MW/m^2]$	$W_{div,out,rise}$ [kJ]	$W_{div,out}$ [kJ]
76697	18-22	S-ELM	23	0.34 ± 0.04	0.56 ± 0.05	35 ± 5	5.8 ± 1.2	42 ± 6
76697	18-22	P-ELM	19	0.47 ± 0.18	0.64 ± 0.07	32 ± 8	6.9 ± 2.9	52 ± 6
79573	14-21	S-ELM	199	0.41 ± 0.12	0.79 ± 0.07	23 ± 5	5.8 ± 1.7	33 ± 6
79573	14-21	P-ELM	12	0.55 ± 0.21	0.77 ± 0.06	30 ± 7	7.1 ± 2.4	48 ± 11

ELM rise time for pellet induced ELMs (0.47±0.18ms) is higher by about 30% in relation to spontaneous ELMs (0.36±0.11ms). At the same time triggered ELMs show a slower decay, which is temporarily almost linear and not exponential in time as for the spontaneous ELMs. As can be seen in figure 6c the ELM rise time does not scale significantly with the pellet size.

The wetted area A_{wet} is usually calculated from IR measurements as $A_{wet} =$

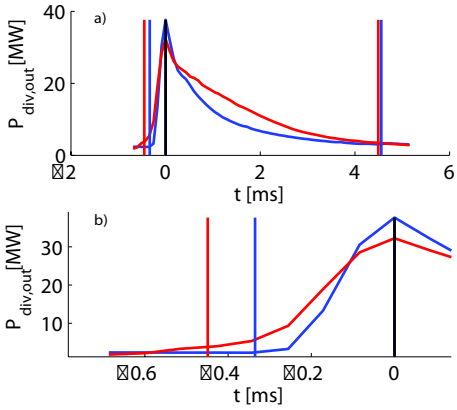

Figure 18. Comparison of power deposition dynamics (Coherent ELM averaging) between spontaneous (blue) and pellet induced ELMs (red) for discharge 76697 (Fueling size pellets / LFS): a) Complete ELM b) ELM rise phase. Vertical lines indicate averages of $t_{ELM,start}$, $t_{ELM,max}$ and $t_{ELM,end}$ for both categories of ELMs

$P_{div,out}/q_{max}$ where q_{max} is the maximum power flux density observed. Assuming a power flux density, which is toroidally symmetrical and which decays radially with a decay length λ, the wetted area A_{wet} is identical to $\lambda\pi(R_1 + R_2)$. Thus in this case A_{wet} gives a good description of the radial decay of the deposition profiles. If there are additional peaks in the deposition profile as it is the case for the pellet induced ELMs in discharge 79573 the quantity A_{wet} has less significance. Accounting for the ELM rise yields for pellet induced ELMs in discharge 76697 slightly higher values for the wetted area on the outer divertor target ($0.56 \pm 0.05m^2$ resp. $0.64 \pm 0.07m^2$) compared to spontaneous ELMs. Thus in this discharge there was a small effect of the pellets on the decay length of the deposition profile at the toroidal angle of the IR observation.

The local temperature increase during an ELM scales with the local power flux density. In discharge 76697, for which we regard the measured profiles of the pellet induced ELMs

as the symmetric component, the maximum power flux density is virtually identical for spontaneous and pellet induced ELMs ($35 \pm 5 MW/m^2$ resp. $32 \pm 8 MW/m^2$). In contrast in discharge 79573 spontaneous ELMs are associated with a lower maximum power flux density compared to the pellet induced ELMs ($23 \pm 5 MW/m^2$ resp. $30 \pm 7 MW/m^2$). This is consistent with the observation, that the additional peaks in the profiles for the pellet induced ELMs in figure 8b are in most cases the absolute maximum in the deposition profile.

In both discharges the energies deposited on the outer divertor $W_{div,rise}$ and W_{div} are higher for the pellet induced ELMs by a factor of 1.2 (1.5 for W_{div} in 79573) compared to spontaneous ELMs. In all cases the corresponding durations are as well higher by an equal or higher factor for the pellet induced ELMs. Thus the higher amount of deposited energy for pellet induced ELMs is mainly caused by a prolongation of the transport phase. Figure 6b) shows that both $W_{div,rise}$ and W_{div} do not show a significant dependence on the pellet size. For completeness we recall that at JET for spontaneous ELMs the energy deposited during the ELM on the outer divertor has been found to scale with the wetted area [9]. As the scatter in wetted area for a given discharge and ELM sort, which has been found in our analysis, is in the order of 10%, we assume that this effect has minor relevance here.

7. Discussion

In this work we have presented various aspects of the associated divertor power load due to pellet induced ELMs and compared the latter with the power load characteristic of spontaneous ELMs and to results from the nonlinear MHD-code JOREK. We have shown that ELMs induced by fueling type pellets injected from the LFS are associated on average with nearly twice as high losses of plasma stored energy as well as radiated energy (measured by bolometry) compared to spontaneous ELMs. For pacing type pellets injected from the VHFS both values have been observed to be rather similar for both categories of ELMs.

Onset and decay of the power flux to the outer divertor are significantly slower for pellet induced ELMs. We speculate that this is associated with a reduced averaged electron and ion temperature of the particles lost during the pellet induced ELMs. The ion parallel transit time is the ratio of the connection length and the ion sound speed. The ELM power load rise time is found to scale with the ion transit time [21]. Since a major fraction of the particles deposited on the divertor during the ELM associated heat flux are suspected to originate from the injected pellet a reduced temperature of such particles and hence a longer deposition time is plausible.

We recall that the ultimate goal of inducing ELMs by pellets is the increase of the ELM frequency (pellet pace making) in conjunction with a corresponding reduction of the power deposited on the plasma facing components [22]. In the light of this the striking feature of pellet induced ELMs to cause an asymmetric divertor power load deserves

particular attention. We have identified a toroidally localised additional peak heat flux (asymmetric component) exceeding the one at the strike line slightly. Furthermore we compared the ELM induced peak heat fluxes and find that the peak heat flux of the symmetric component of pellet induced ELMs and the one of spontaneous ELMs are similar. The total peak heat flux from both components of pellet induced ELMs is found to be considerably larger than the one for spontaneous ELMs. It is not clear, if the asymmetric component is of similar extent for ELMs induced by pellets injected from the high field side or ELMs induced by smaller pellets.
The increase of the ELM frequency is observed to cause a reduced ELM loss size, when ELM pace making is successful, as e.g. shown for AUG [22] or DIII-D [23]. From the current understanding not only the reduction of the ELM associated peak heat flux at an arbitrary toroidal location in the divertor but also the heat flux at the position, where it peaks in toroidal and radial direction, need to be demonstrated to be reduced when the ELM energy loss in the pedestal is reduced.

Acknowledgments

This work was supported by EURATOM and carried out within the framework of the European Fusion Development Agreement. The views and opinions expressed herein do not necessarily reflect those of the European Commission. The authors would like to thank G. Kocsis for very fruitful discussions.

8. References

[1] Zohm H 1996 *Plas.Phys.Contr.Fusion* **38** 105–128
[2] Federici G *et al* 2003 *J.Nucl.Mater.* **313-316** 11–22
[3] Loarte A *et al* 2003 *J.Nucl.Mater.* **313-316** 962–966
[4] Eich T *et al* 2005 *J.Nucl.Mater.* **337-339** 669–676
[5] Lang P *et al* 2003 *Nuclear Fusion* **43**
[6] Herrmann A *et al* 2002 *Plas.Phys.Contr.Fusion* **44** 883–903
[7] Geraud A *et al* 2007 *Fusion Engineering and Design* **82** 2183 – 2188
[8] Lang P *et al* 2011 *Nuclear Fusion* **51** 033010
[9] Eich T *et al* 2010 DOI: 10.1016/j.jnucmat.2010.11.079 *Journal of Nuclear Materials*
[10] Herrmann A *et al* 1995 *Plas.Phys.Contr.Fusion* **37** 17–26
[11] Alper B *et al* 2010 *37th EPS Conference on Controlled Fusion and Plasma Physics*
[12] Pégourié B, Waller V, Nehme H, Garzotti L, and Géraud A 2007 *Nuclear Fusion* **47** 44
[13] Solano E R *et al* 2008 *Nuclear Fusion* **48** 065005
[14] Eich T *et al* 2003 *Phys.Rev.Letter* **91** 195003
[15] Punjabi A *et al* 1992 *Phys. Rev. Lett.* **69** 3322–3325
[16] Kocsis G *et al* 2007 *Nuclear Fusion* **47** 1166
[17] Jachmich S *et al* 2007 *34th EPS Conference on Controlled Fusion and Plasma Physics*
[18] Huysmans G T A, Pamela S, van der Plas E, and Ramet P 2009 *Plas.Phys.Contr.Fusion* **51** 124012
[19] Czarny O and Huysmans G 2008 *Journal of Computational Physics* **227** 7423 – 7445
[20] Huysmans G *et al* 2010 *IAEA Fusion Energy Conference, Daejeon, Korea*

[21] Eich T *et al* 2003 *J.Nucl.Mater.* **313-316** 919–924
[22] Lang P *et al* 2004 *Nuclear Fusion* **44** 665–677
[23] Baylor L R *et al* 2010 *37th EPS Conference on Controlled Fusion and Plasma Physics*